Journal of Metals, Materials and Minerals, 36(3), e2647, 2026

Role of alkali and alkaline-earth doped in zeolite A-derived from industrial waste toward direct ethanol dehydrogenation to acetaldehyde

Darunee SUKCHIT[1], Malee PRAJUABSUK[1], Chan INNTAM[1], Saisamorn LUMLONG[1], Bongkochawan PAKAMWONG[1], Auradee PUNKVANG[2], Duangkamol GLEESON[3], Pantita TRONGJITRAKSA[4], Paramasivam SHANMUGAM[5], Supakorn BOONYUEN[5], Niramol JUNTARACHAT[6], Sasijuta WATTANARACH[7], Parjaree THAVORNITI[7], Bunjerd JONGSOMJIT[8,9], and Pornpan PUNGPO[1,*]

[1] *Department of Applied Chemistry and Center of Excellence for Innovation in Chemistry, Faculty of Science, Ubon Ratchathani University, Ubon Ratchathani 34190, Thailand*
[2] *Division of Chemistry, Faculty of Science, Nakhon Phanom University, Nakhon Phanom 48000, Thailand*
[3] *Applied Computational Chemistry Research Unit and Department of Chemistry, School of Science, King Mongkut's Institute of Technology Ladkrabang, Bangkok 10520, Thailand*
[4] *Department of Chemical Engineering, Faculty of Engineering, King Mongkut's University of Technology Thonburi, Bangkok 10140, Thailand*
[5] *Department of Chemistry, Faculty of Science and Technology, Thammasat University, Pathum Thani 12120, Thailand*
[6] *Faculty of Engineering, Thaksin University, Phattalung 93210, Thailand*
[7] *National Metal and Materials Technology Center, National Science and Technology Development Agency (NSTDA), Pathum Thani 12120, Thailand*
[8] *Center of Excellence on Catalysis and Catalytic Reaction Engineering, Department of Chemical Engineering, Faculty of Engineering, Chulalongkorn University, Bangkok 10330, Thailand*
[9] *Bio-Circular-Green-Economy Technology & Engineering Center, BCGeTEC, Department of Chemical Engineering, Faculty of Engineering, Chulalongkorn University, Bangkok 10330, Thailand*

***Corresponding author e-mail**: pornpan.p@ubu.ac.th

Received date:
26February 2026
Revised date:
21 March 2026
Accepted date:
3 May 2026

Keywords:
Zeolite A;
Alkali;
Alkaline earth;
Ethanol dehydrogenation;
Acetaldehyde

Abstract

In this study, a sustainable catalytic route for converting ethanol into value-added acetaldehyde was developed using alkali- and alkaline earth-modified zeolite A synthesized from sugarcane bagasse ash (SCBA). Zeolite A was first prepared via alkaline fusion followed by hydrothermal crystallization and subsequently doped with 1 wt% K^+ or Ca^{2+} using incipient wetness impregnation. Comprehensive physicochemical characterization (X-ray fluorescence (XRF), X-ray diffraction (XRD), scanning electron microscopy with energy-dispersive X-ray spectroscopy (SEM-EDX), Fourier transform infrared spectroscopy (FTIR), nitrogen physisorption (N_2 physisorption), ammonia temperature-programmed desorption (NH_3-TPD), and carbon dioxide temperature-programmed desorption (CO_2-TPD)) confirmed the formation of a highly crystalline LTA framework with tunable acid-base properties upon cation incorporation. Catalytic evaluation demonstrated that ethanol dehydrogenation strongly depends on the balance of surface acid-base sites. The parent and Ca-modified zeolite A exhibited moderate acetaldehyde selectivity (11.2% and 21.2%, respectively), likely due to competing dehydration reactions. In contrast, K-modified zeolite A achieved higher acetaldehyde selectivity (51.8%) at 35.2% ethanol conversion, attributed to enhanced surface basicity and suppressed acidity. Mechanistic analysis suggests that K^+ and Ca^{2+} promote ethanol dehydrogenation by facilitating ethoxide formation and β-hydrogen elimination on basic lattice oxygen sites. These findings demonstrate a cost-effective, noble-metal-free catalytic strategy and highlight the potential of SCBA-derived zeolite A as a sustainable platform for green ethanol upgrading.

1. Introduction

The sustainable production of chemicals has gained significant momentum as global industries seek to transition toward low-carbon and environmentally responsible processes. Central to this shift is the development of biomass-derived platform chemicals that can reduce reliance on fossil carbon inputs [1]. Among these renewable feedstocks, ethanol produced from agricultural wastes stands out as a versatile and abundant chemical precursor. Its catalytic transformation enables the generation of numerous industrial intermediates, including acetic acid, ethylene, ethyl acetate, diethyl ether and acetaldehyde [2]. Among these products, acetaldehyde holds particular importance as it serves as a key building block in the manufacture of ethyl acetate, acetic acid, acetic anhydride, pyridines, and isobutanol [3].

Acetaldehyde is generally produced via the Wacker oxidation of petrochemical ethylene using $PdCl_2$ and $CuCl_2$ catalysts [4-7]. The

heavy dependence on noble metals as well as non-renewable ethylene underscores the need for greener and more sustainable alternatives. An attractive route involves the dehydrogenation of ethanol, a renewable and widely available resource obtained through biomass fermentation [8]. Ethanol can be converted into acetaldehyde through two primary catalytic pathways: selective oxidation and non-oxidative dehydrogenation [9-12]. The latter route requires no external oxidant and simultaneously generates hydrogen as a valuable co-product, positioning ethanol dehydrogenation as a promising technology within integrated biorefinery and hydrogen-economy frameworks.

Zeolites have emerged as appealing catalysts for ethanol dehydrogenation due to their high surface areas, shape selectivity, excellent cation-exchange properties, and tunable acid-base characteristics [13,14]. Among them, zeolite A ($Na_{12}[AlO_2SiO_2]_{12}\cdot 27H_2O$) is one of the most structurally versatile materials. Its cubic LTA framework with a 1:1 Si/Al ratio provides a high density of framework aluminum atoms and charge-balancing sodium ions, resulting in exceptional ion-exchange capacity [15-17]. These characteristics make zeolite A a robust platform for catalytic modification aimed at controlling acidity and basicity-key factors determining ethanol conversion pathways.

A wide range of transition-metal catalysts, including copper [18-21], magnesium [22,23], nickel [24-26], zinc [19,27,28], and gold [25,29-32], has been explored for ethanol dehydrogenation. Generally, such catalysts fall into two categories: (i) metals such as Cu, Ag, Pd, and Au, and (ii) metal oxides including CuO, ZnO, MgO, and Cr_2O_3 [33]. While effective, these systems face limitations arising from high cost, metal scarcity, and environmental burdens associated with mining and disposal. As a result, there is increasing interest in cost-effective, noble-metal-free catalytic systems derived from more abundant and sustainable elements [34].Alkali and alkaline-earth cations have gained attention as alternatives, yet their potential to selectively promote ethanol dehydrogenation-especially when supported on zeolite A synthesized from sugarcane bagasse ash, remains insufficiently explored [35,36].

Sugarcane bagasse ash is an agricultural waste rich in reactive amorphous silica, offering a sustainable and low-cost precursor for zeolite synthesis [37-40]. Converting SCBA into zeolite A aligns well with circular-economy principles Importantly, recent studies suggest that ash-derived synthesis can promote the formation of hierarchical porosity, which enhances the accessibility of bulky molecules to the active sites. However, no systematic study has elucidated how simple non-redox alkali (K^+) and alkaline-earth (Ca^{2+}) cations incorporated into SCBA-derived zeolite A influence acid-base properties and catalytic performance in ethanol dehydrogenation [22,41]. Most reported systems rely on transition metals, leaving the role of these inexpensive cations in controlling acetaldehyde selectivity largely unexplored.

Therefore, this study aims to synthesize zeolite A from sugarcane bagasse ash and modify it with K^+ and Ca^{2+} cations to evaluate their influence on surface acidity-basicity, structural properties, and catalytic behavior in ethanol dehydrogenation. Through comprehensive physico-chemical characterization and vapor-phase catalytic testing, we elucidate how non-redox cations modulate the LTA framework to enhance acetaldehyde formation.

The novelty of this work lies in introducing a completely noble-metal-free catalytic concept in which non-redox alkali K^+ and alkaline-earth Ca^{2+} cations function as the active species. By modulating the surface basicity and framework environment, these inexpensive cations provide an alternative pathway to traditional redox-active metals. By integrating waste-valorized zeolite A with simple, inexpensive cation modification, this study provides a new sustainable, low-cost strategy for selective ethanol dehydrogenation. The findings offer valuable insights into acid-base tuning in zeolites and establish a new pathway for green acetaldehyde production. This approach effectively shifts the paradigm from energy-intensive, metal-based catalysis toward simpler, earth-abundant cation systems for ethanol upgrading.

2. Experimental

2.1 Materials

Analytical grade reagents used in this work were $NaAlO_2$ (anhydrous, Al (Al_2O_3): 50% to 56%, Na (Na_2O): 37% to 45%, Sigma-Aldrich, USA), NaOH (≥ 97.0%, Carlo Erba Reagents, France), KOH (≥ 85.0%, Merck, Germany), $CaCl_2$ (≥ 96.0%, Sigma-Aldrich, USA) and Ethanol (≥99.5%, Supelco).

2.2 Synthesis of zeolite A

Sugarcane bagasse ash (10 g) was first homogenized with NaOH pellets (12 g), corresponding to a NaOH-to-ash weight ratio of 1.2, to provide a strong alkaline environment for effective dissolution of silica and alumina species during zeolite formation. The mixture was mechanically ground for 10 min to ensure uniformity and then transferred to a crucible for alkaline fusion. The fusion process was heated at 550°C for 90 min using a muffle furnace and allowed to cool at room temperature. To achieve a target SiO_2/Al_2O_3 molar ratio of approximately 1, an appropriate amount of $NaAlO_2$ was added to the fused material. The resulting mixture was further ground for 15 min and transferred to a polypropylene container. Deionized water was then added for obtaining a liquid-to-solid ratio of 4.5. Hydrothermal crystallization was conducted by heating the slurry at 90 °C for 16 h in an oven. Samples were collected, thoroughly washed with deionized water and filtered. Finally, the material was dried at 90°C for 16 h. The synthesized sample was denoted as zeolite A [42].

2.3 Preparation of catalysts

Potassium and calcium-modified zeolite A catalysts were prepared via the incipient wetness impregnation method with a nominal metal loading of 1.0 wt%. Prior to impregnation, the pore volume of the support was determined experimentally and found to be 3.10 mL for 2 g of zeolite A. The required amounts of potassium hydroxide (KOH) or calcium chloride ($CaCl_2$) were calculated to achieve a metal loading of 1.0 wt% and dissolved in 3.10 mL of deionized water. The resulting solution was added dropwise onto 2 g of the zeolite support under continuous stirring to ensure uniform distribution. After impregnation, the samples were aged at room temperature for 12 h, followed by drying at 110°C for 24 h to remove residual moisture. The dried samples were then calcined at 400°C for 4 h under air atmosphere, with a heating rate of $5°C\cdot min^{-1}$ [43]. The prepared catalysts were denoted as K-zeolite A and Ca-zeolite A. KOH and $CaCl_2$ were selected due to their high solubility and widespread use in zeolite modification. Although different

anions (OH^- and Cl^-) were employed, all samples were subjected to identical calcination conditions, which are expected to effectively remove or decompose residual anionic species. Therefore, their influence on the final catalyst properties is considered negligible. Although calcination at 400°C is expected to remove residual chloride species, we acknowledge that trace Cl^- may still influence surface properties. However, no characteristic Cl-related phases were detected in XRD, and the acid-base trends observed from NH_3-TPD and CO_2-TPD are consistent with cation effects rather than precursor anions.

2.4 Characterization of catalyst

Composition of sugarcane bagasse ash was determined by wavelength-dispersive X-ray fluorescence spectroscopy (XRF), (ZSX Primus II, Rigaku, USA). The crystalline phases of the catalysts were identified by X-ray diffraction (XRD) on a Siemens D5000 diffractometer equipped with Cu Kα radiation (Ni filter), 2θ range of 5° to 80°, step size of 0.04° and scanning rate of 0.5 s per step. Morphological propriety was examined by scanning electron microscopy (SEM), (Hitachi S-3400N). Elemental composition and spatial distribution were determined by energy-dispersive X-ray spectroscopy (EDX), (Link Isis Series 300). Functional groups were identified by Fourier-transform infrared spectroscopy (FTIR), (Nicolet 6700) over wave-number range of 400 cm^{-1} to 4000 cm^{-1}. Textural properties, including surface area and porosity, were evaluated using a Quantachrome Autosorb IQ3 analyzer. The BET surface area was derived from nitrogen adsorption-desorption isotherms measured at –196°C after degassing under vacuum at 150°C for 4 h. Pore volume and pore size distribution were calculated using the Barrett-Joyner-Halenda (BJH) method. The acidity and acid strength were examined via ammonia temperature-programmed desorption (NH3-TPD) using a Micromeritics Chemisorb 2750 system. In this procedure, 0.1 g of catalyst was loaded on quartz wool in a U-tube reactor, pretreated in helium at 250°C for 1 h, followed by NH_3 adsorption at 40°C. After removing physisorbed ammonia, chemisorbed species were desorbed by heating from 40°C to 800°C with a rate of 10°C·min^{-1} and helium flowrate of 25 mL·min^{-1}. Desorbed NH_3 was quantified using a thermal conductivity detector (TCD). Basicity measurements were carried out under similar conditions using CO_2-TPD, replacing ammonia with CO_2 as the probe molecule [43].

2.5 Reaction study

The catalytic performance was evaluated for ethanol dehydrogenation in a continuous-flow fixed-bed glass microreactor placed inside an electric furnace. In each experiment, 0.1 g of catalyst was packed in the central section of the reactor and held in place with 0.015 g of quartz wool to ensure proper fixation and uniform gas distribution. Prior to the reaction, the catalyst was pretreated under a nitrogen atmosphere (60 mL·min^{-1}) at 200°C for 1 h to remove physically adsorbed moisture and impurities. Ethanol was fed using a syringe pump at a flow rate of 0.397 mL·h^{-1} and vaporized at 120°C before entering the reactor. Nitrogen was used as a carrier gas at a constant flow rate of 60 mL·min^{-1}, resulting in a weight hourly space velocity (WHSV) of 3.11 gethanol/gcatalysth. The reaction was conducted at atmospheric pressure over a temperature range of 200°C to 400°C using a stepwise temperature program.

At each reaction temperature, the system was maintained for 30 min prior to product sampling to allow stabilization of the catalytic performance. Subsequently, three product samples were collected at each temperature, and the reported values represent the average of these measurements. Each catalytic experiment was repeated at least three times to ensure reproducibility, and the corresponding error bars were added to the catalytic performance plots to represent the experimental variation.

The reaction products were analyzed using a gas chromatograph (Shimadzu GC-14B) equipped with a flame ionization detector (FID) and a DB-5 capillary column maintained at 150°C. Product identification and quantification were carried out using external calibration with standard compounds. A schematic representation of the experimental setup for ethanol dehydrogenation is shown in Scheme 1. Ethanol conversion, product selectivity, and product yield were calculated according to Equation (1)-(3), respectively [1,43,44], based on gas-phase species only. The GC analysis confirmed the presence of unreacted ethanol and gaseous products, enabling the calculation of ethanol conversion from the inlet and outlet gas-phase compositions.

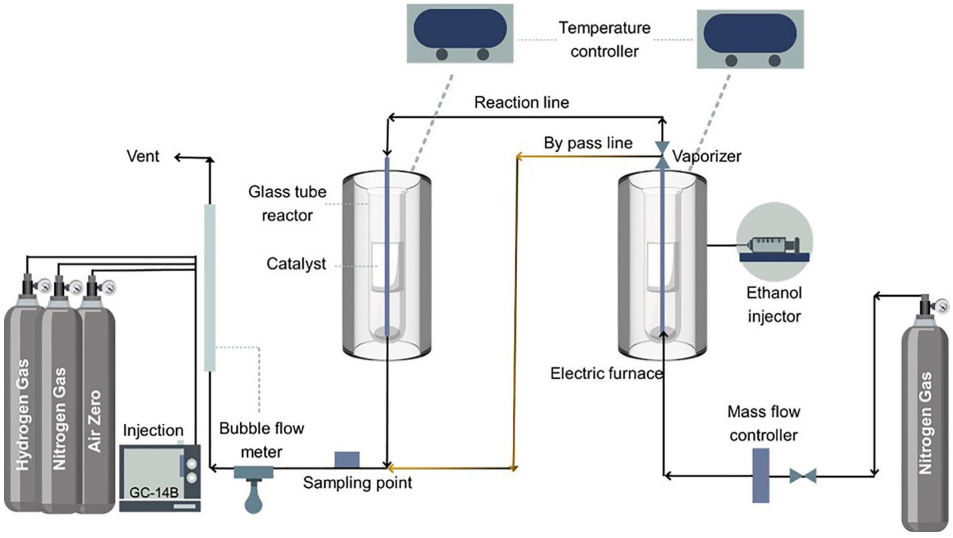

Scheme 1. Ethanol dehydrogenation reaction system.

$$\text{Ethanol conversion}: X_{EtOH}\ (\%) = \frac{mol_{EtOH}\ (in) - mol_{EtOH}\ (out)}{mol_{EtOH}\ (in)} \times 100 \quad (1)$$

$$\text{Selectivity of product}: S_i\ (\%) = \frac{mol_i}{\sum mol_i} \times 100 \quad (2)$$

$$\text{Yield of product}: Y_i\ (\%) = \frac{X_{EtOH} \times S_i}{100} \quad (3)$$

Where $mol_{EtOH}\ (in)$, $mol_{EtOH}\ (out)$ and mol_i are moles of ethanol in feed, moles of unreacted ethanol and moles of each product, respectively.

3. Results and discussion

3.1 Characterization of catalysts

The chemical composition of sugarcane bagasse ash (SCBA) and synthesized zeolite A, along with K and Ca modified zeolites, is presented in Table 1. SCBA mainly consisted of SiO_2 (74.4%), with minor amounts of Al_2O_3, CaO, Fe_2O_3, SO_3, K_2O, and MgO, indicating its suitability as a silica-rich precursor for zeolite A synthesis. After hydrothermal treatment, zeolite A showed a significant increase in Al_2O_3 content (36.2%) and a high Na_2O concentration (15.7%), while K_2O, CaO, and MgO decreased, reflecting the structural incorporation of Al and Na during crystallization. Modification with K or Ca resulted in increased K_2O (2.57%) or CaO (4.17%), respectively, with slight changes in Na_2O, demonstrating effective ion exchange without disturbing the Si/Al framework. These results highlight the potential of zeolite A from SCBA as a tunable material for catalytic applications. The successful synthesis of zeolite A from SCBA was confirmed by the chemical composition, showing a Si/Al ratio of 1.17, consistent with the characteristic LTA framework [14]. The incorporation of aluminum and sodium into the framework indicates proper crystallization, while subsequent K^+ or Ca^{2+} modification adjusted the impregnated cations without altering the Si/Al ratio. These results demonstrate the formation of well-defined zeolite A with tunable cation sites for catalytic applications.

The XRD patterns of the synthesized zeolite A and its impregnated forms (K-Zeolite A and Ca-Zeolite A) are presented in Figure 1. The diffraction peaks of zeolite A exhibit characteristic reflections at 2θ values of 7.2°, 10.2°, 12.5°, 16.1°, 21.7°, 24.0°, 27.2°, 30.0°, 32.6°, and 34.2°. These results are consistent with the standard JCPDS card No. 39-0222, confirming the successful formation of zeolite A with a cubic LTA structure [45,46]. After impregnation with potassium and calcium ions, the primary diffraction peaks of zeolite A remain unchanged, indicating that the crystal framework was well-preserved. However, minor additional peaks were observed at 32.9° for K-zeolite A and 32.2° for Ca-zeolite A, which are assigned to the K_2O (JCPDS No. 26-1327) and CaO (JCPDS No. 37-1497) phases, respectively [47-50]. The detection of these oxide phases, further supported by the XRF results showing approximately 1.1 wt% of K_2O and CaO, suggests the successful incorporation of metal species onto the zeolite surface without compromising its structural integrity.

The SEM analysis of the synthesized zeolite A and its modified forms is presented in Figure 2. The synthesized zeolite A exhibits well-defined cubic crystals with smooth surfaces and a uniform particle size in the range of 2 µm to 5 µm, consistent with the LTA-type zeolite structure [51,52]. After impregnation with potassium and calcium ions, the cubic morphology is generally retained, indicating that the modification process does not disrupt the crystalline framework. However, slight surface roughness and the presence of small agglomerates are observed in the K and Ca-modified samples. These features are attributed to the presence of surface-associated K and Ca-containing species introduced during the impregnation process.

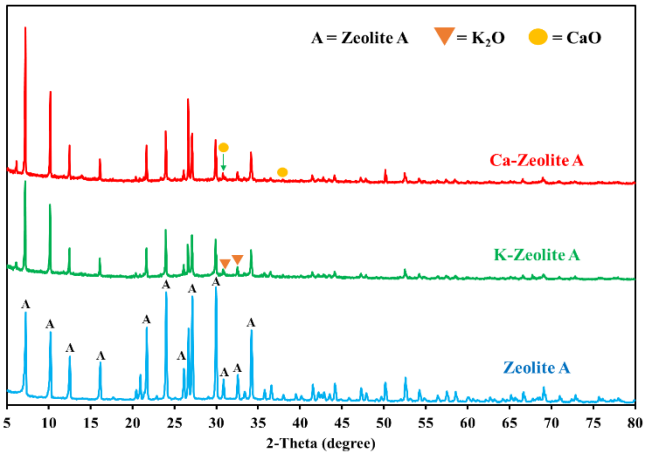

Figure 1. X-ray diffraction patterns of zeolite A, K-zeolite A, and Ca-zeolite A catalysts.

Table 1. Chemical composition (wt%) of sugarcane bagasse ash, zeolite A, and modified zeolite A determined by X-ray fluorescence (XRF).

Component (% by weight)	SiO_2	Al_2O_3	CaO	Fe_2O_3	SO_3	Na_2O	K_2O	MgO	Others
Sugarcane bagasse ash	74.40	3.55	3.57	1.42	1.12	-	7.92	3.08	4.94
Zeolite A	42.50	36.20	2.54	0.48	0.03	15.70	1.10	1.08	0.37
K/Zeolite A	42.12	36.34	1.93	0.50	0.19	15.10	2.57	0.92	0.33
Ca/Zeolite A	40.33	36.13	4.17	0.46	0.10	14.60	1.03	0.85	2.33

Table 2. Elemental distribution (wt.%) on the external surface of catalysts obtained from EDX.

Sample	%Si	%Al	%O	%Na	%K	%Ca	Si/Al
Zeolite A	26.15	24.63	27.62	12.96	0.8	1.4	1.06
K-zeolite A	23.15	21.68	31.79	13.00	2.02	1.33	1.06
Ca-zeolite A	24.32	22.71	29.12	12.27	0.82	2.57	1.07

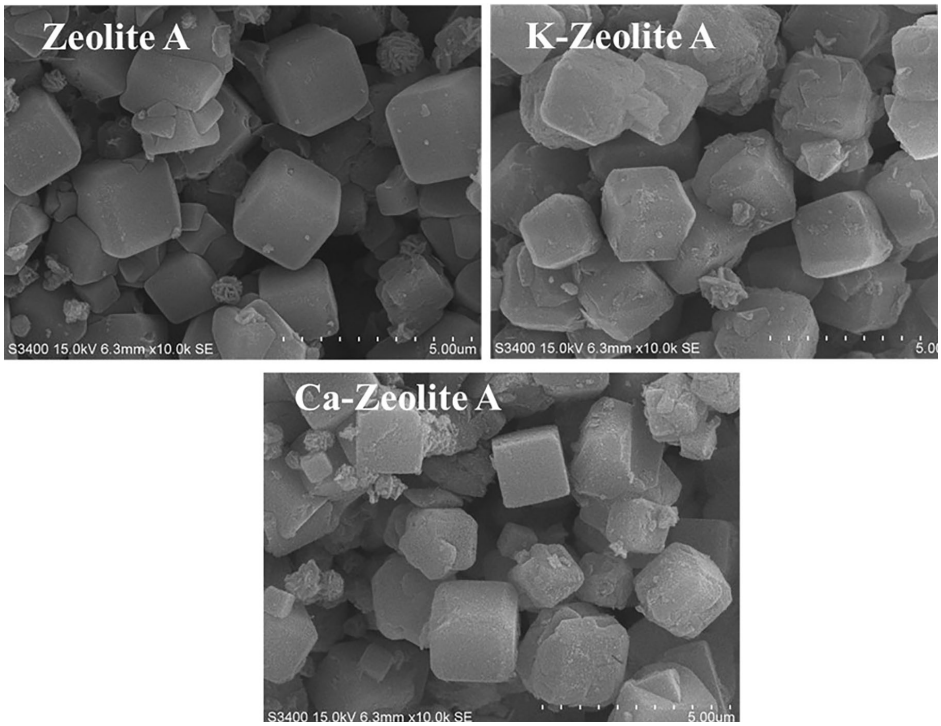

Figure 2. SEM images of zeolite A, K-zeolite A, and Ca-zeolite A catalysts.

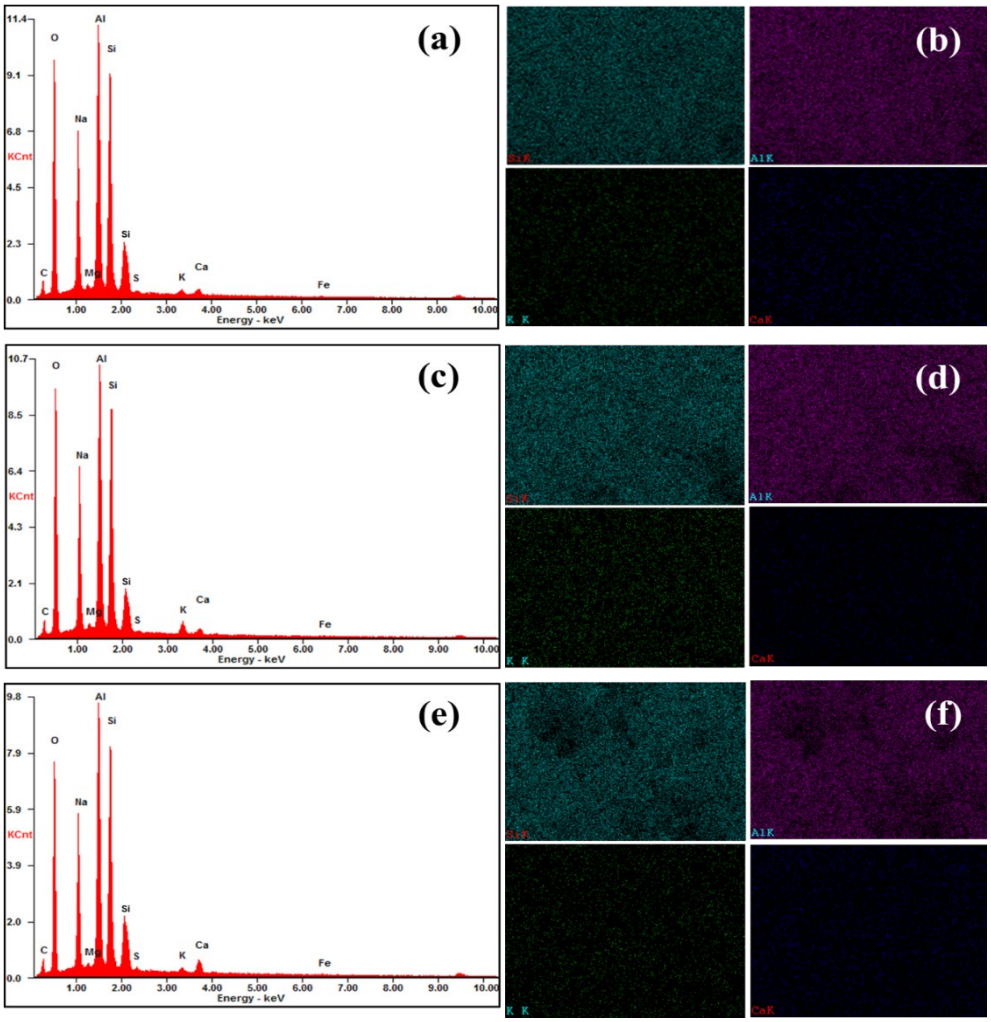

Figure 3. EDX spectra and corresponding elemental mapping images of (a, b) zeolite A, (c, d) K-impregnated zeolite A, and (e, f) Ca-impregnated zeolite A.

These morphological changes are consistent with the XRD results, which indicate that the zeolite framework remains intact after modification. Thus, the modification primarily affects the surface characteristics while preserving the overall structure of zeolite A. The EDX spectra (Figure 3(a,c,e) confirm that Si, Al, and O are the dominant framework elements of zeolite A. The spectrum of pristine zeolite A (Figure 3(a)), included as a control, shows only trace amounts of K and Ca species. In contrast, the intensities of K and Ca signals are noticeably enhanced in the modified samples, verifying the successful incorporation of potassium and calcium species onto the zeolite A surface. As summarized in Table 2, the Si/Al ratio remains nearly constant (1.06 to 1.07) after modification, indicating that the framework structure of zeolite A is well preserved during the impregnation process. The corresponding elemental mapping images (Figure 3(b,d,f) further demonstrate that Si, Al, O, and the introduced K and Ca species are uniformly distributed across the zeolite particles. This homogeneous dispersion suggests the absence of significant metal aggregation and confirms effective interaction between the impregnated species and the zeolite framework. Such uniform distribution of K and Ca is particularly important for catalytic performance, as it ensures the formation of well-dispersed basic sites and enhances metal-support interactions. These features are expected to improve the accessibility and uniformity of active sites, thereby facilitating ethanol dehydrogenation to acetaldehyde while maintaining the structural integrity of zeolite A under reaction conditions. The peak observed at around 2.0 keV is attributed to the Si Kβ emission, appearing as a secondary Si peak adjacent to the main Si Kα peak (~1.74 keV), consistent with the aluminosilicate framework of zeolite A.

The FTIR spectra of zeolite A, K-zeolite A, and Ca-zeolite A are shows in Figure 4. All zeolites exhibited characteristic absorption bands, corresponding to the LTA-type zeolite framework. The broad band at 3450 cm^{-1} to 3550 cm^{-1} and the band at 1650 cm^{-1} correspond to the O-H stretching vibration of water molecules adsorbed within zeolite cavity. The strong bands observed in the range of 950 cm^{-1} to 1000 cm^{-1} are attributed to the asymmetric stretching vibrations of the (Si, Al)-O-T (T = Si or Al) bonds in the aluminosilicate framework. The bands at approximately 660 cm^{-1} to 700 cm^{-1} correspond to the double four-ring (D4R) structural units, which are typical of the LTA framework. Additionally, the absorption bands around 550 cm^{-1} to 460 cm^{-1} correspond to the vibrations of the T-O-T linkages [53,54].

The LTA structure of zeolite A was preserved during K^+ and Ca^{2+} ion exchange process since the presence of all characteristic peaks. However, slight shifts in the O-H and (Si, Al)-O bands were observed, indicating weak interactions of exchanged cations and the zeolite framework. These results suggest that the incorporation of K^+ and Ca^{2+} ions did not alter the crystalline structure of zeolite A.

The N_2 adsorption-desorption isotherms and corresponding textural parameters are presented in Figure 5 and Table 3. All samples exhibit Type IV isotherms with H3-type hysteresis loops, indicating the presence of secondary mesoporosity, which is attributed to interparticle voids formed during the aggregation and crystallization of ash-derived precursors [55,56]. These mesoporous features reflect external textural characteristics rather than a transformation of the intrinsic zeolitic framework.

The parent zeolite A shows a relatively low BET surface area (10.4 $m^2 \cdot g^{-1}$), which is significantly lower than the typical values reported for conventional zeolite A (400 $m^2 \cdot g^{-1}$ to 600 $m^2 \cdot g^{-1}$). However, it is well recognized that N_2 adsorption at 77 K is not suitable for accurately probing the microporosity of LTA-type zeolites, due to the restricted diffusion of N_2 molecules into the small pore apertures (0.4 nm). Consequently, the measured BET surface area underestimates the intrinsic microporous structure. In addition, residual species originating from sugarcane bagasse ash (SCBA) may further limit pore accessibility.

To further assess the pore structure, t-plot analysis was performed (Table 3). The results indicate that K-zeolite A and Ca-zeolite A exhibit measurable micropore areas of 17.8 $m^2 \cdot g^{-1}$ and 14.2 $m^2 \cdot g^{-1}$, respectively, suggesting partial accessibility of the microporous network after modification.

The increase in BET surface area following K^+ and Ca^{2+} modification (to ~30 $m^2 \cdot g^{-1}$) can be attributed to the partial removal of pore-blocking species and/or rearrangement of surface aggregates during impregnation and calcination, which improves pore accessibility. Similar behavior has been reported in modified zeolitic and alumino-silicate materials, where thermal treatment and metal incorporation enhance the exposure of accessible surface sites. Meanwhile, the decrease in average pore size (from 13.5 nm to 4.5 nm to 5.3 nm) may result from the deposition of cations or oxide clusters near mesopore walls or pore entrances, effectively narrowing interparticle voids. Such pore narrowing or partial pore occupation after metal incorporation has also been widely observed in related systems [57-59].

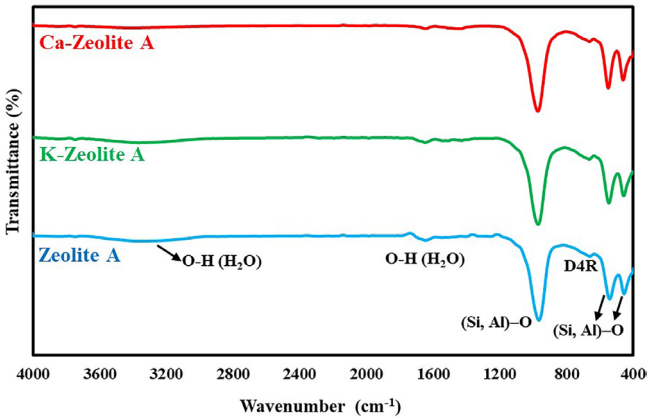

Figure 4. FTIR spectra of zeolite A, K-zeolite A, and Ca-zeolite A catalysts.

Table 3. Surface area, pore volume, and hierarchical porosity distribution of the catalysts studied in this work.

Catalysts	S_{BET} [$m^2 \cdot g^{-1}$]	S^a_{micro} [$m^2 \cdot g^{-1}$]	V_{Total} [$cm^3 \cdot g^{-1}$]
Zeolite A	10.4	N/A*	0.04
K/Zeolite A	29.5	17.8	0.03
Ca/Zeolite A	29.9	14.2	0.04

[a] Calculated via t-plot method.
*Micropore accessibility in parent zeolite A was restricted at 77 K.

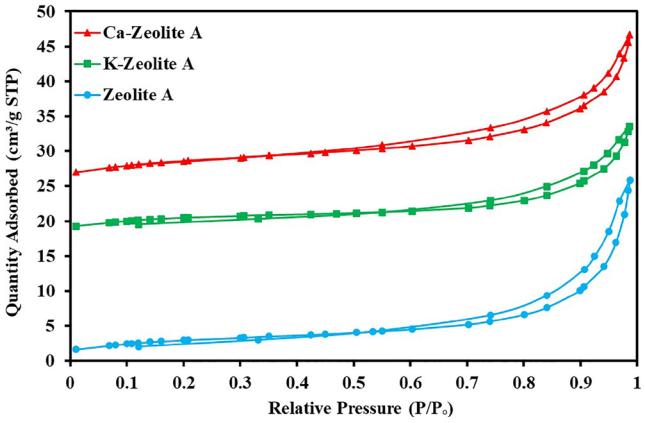

Figure 5. N_2 adsorption-desorption isotherm of the zeolite A, K-zeolite A, and Ca-zeolite A catalysts.

These results indicate that although micropore accessibility is partially restricted under N_2 adsorption conditions, the material retains its intrinsic zeolitic framework (as confirmed by XRD and FTIR), while the presence of secondary mesoporosity enhances mass transfer, contributing to improved catalytic performance.

Figure 6 presents the NH_3-TPD profiles and peak deconvolution results of the parent and modified catalysts. Based on the NH_3 desorption temperature ranges, the desorption peaks were classified into weak acid sites (< 200°C), medium acid sites (200°C to 400°C), and strong acid sites (> 400°C) [43,60]. The parent zeolite A exhibits multiple desorption features centered at approximately 140°C to 200°C and 400°C, corresponding to weak, medium, and high-temperature NH_3 desorption species associated with framework-related acidic sites in the LTA structure.

After metal impregnation, noticeable changes in both the total acidity and the distribution of acid sites were observed (Table 4). K-zeolite A exhibited increased weak and medium acid sites, while the contribution of high-temperature NH_3 desorption species decreased compared with the parent zeolite A, suggesting that potassium modification altered the distribution and strength of acidic sites through interaction with framework charge-compensating cations. In contrast, Ca-zeolite A retained significant contributions from medium and high-temperature desorption species, resulting in a relatively balanced acid-site distribution and a high total acidity value (2509.7 μmol $NH_3/g_{catalyst}$).

The deconvolution analysis further indicates that the incorporation of K^+ and Ca^{2+} modified the acid-site distribution of zeolite A, most likely through partial ion exchange with framework charge-compensating cations. These changes in acidity distribution are expected to influence the catalytic performance by altering the accessibility and strength of the acidic sites.

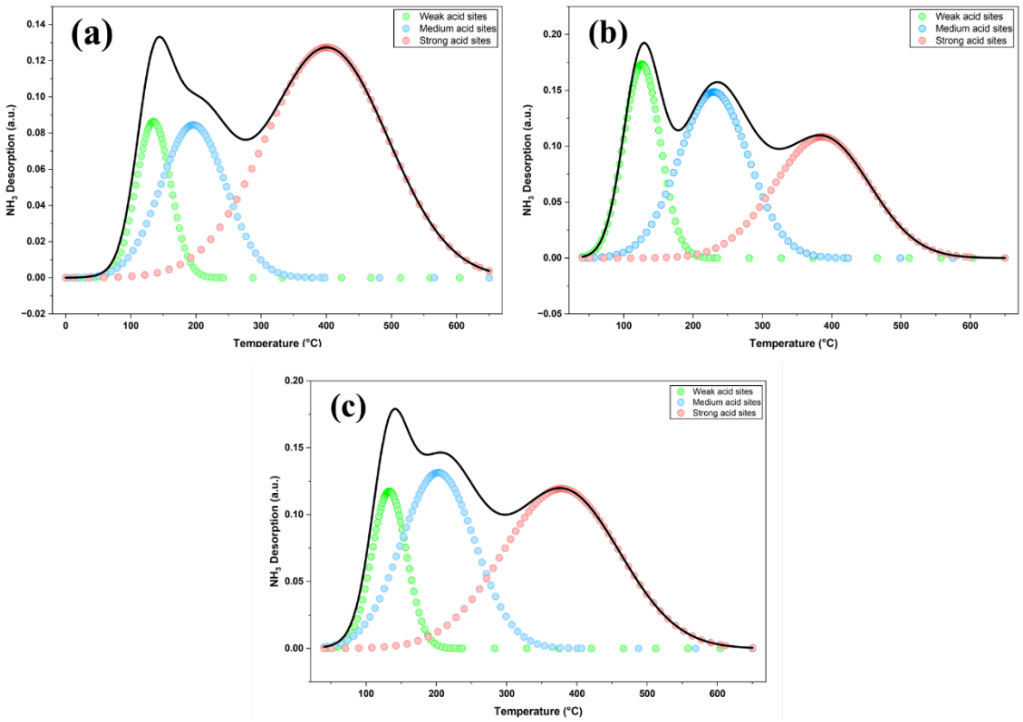

Figure 6. NH_3-TPD profiles and peak deconvolution of zeolite A (a), K-zeolite A (b), and Ca-zeolite A (c). The desorption peaks were classified into three categories: weak acid sites, medium acid sites, and strong acid sites.

Table 4. Number of acid sites of all samples obtained from NH_3-TPD.

Adsorbents	**Number of acid sites [μmole $NH_3/g_{catalyst}$]**			
	Weak acid sites	**Medium acid sites**	**Strong acid sites**	**Total acid sites**
Zeolite A	295.3	548.2	1551.6	2395.1
K-Zeolite A	600.7	974.3	971.0	2546.0
Ca-Zeolite A	370.8	877.7	1261.2	2509.7

Table 5. Number of basic sites of all samples obtained from CO_2-TPD.

Samples	Number of base sites [µmole $CO_2/g_{catalyst}$]			
	Weak base sites	**Medium base sites**	**Strong base sites**	**Total base sites**
Zeolite A	10.6	2.7	78.9	92.2
K-Zeolite A	56.9	91.4	68.1	216.4
Ca-Zeolite A	16.9	1.2	54.7	72.8

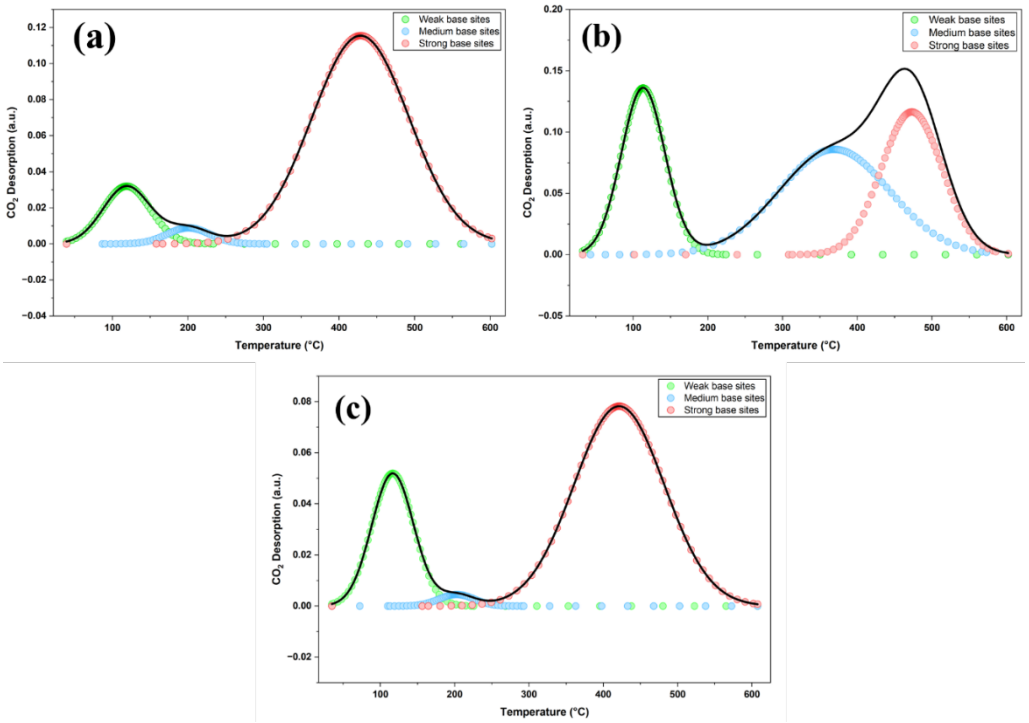

Figure 7. CO_2-TPD profiles and peak deconvolution of zeolite A (a), K-zeolite A (b), and Ca-zeolite A (c). The desorption peaks were classified into three categories: weak base sites, medium base sites, and strong base sites.

The CO_2-TPD profiles and corresponding deconvolution results are presented in Figure 7, while the quantitative distribution of base sites is summarized in Table 5. Based on the CO_2 desorption temperature ranges, the desorption peaks were classified into weak base sites (< 200°C), medium base sites (200°C to 400°C), and strong base sites (> 400°C). The low-temperature desorption peaks are attributed to weak basic sites associated with surface hydroxyl groups and weakly bound oxygen species, whereas the higher-temperature desorption peaks are associated with more strongly bound CO_2 species related to framework oxygen atoms and cation-associated basic sites in the zeolite structure [61].

The parent zeolite A exhibits desorption features centered at approximately 120°C and 420°C, corresponding to weak and strong basic sites, respectively, with only a minor contribution from medium base sites. After modification, noticeable changes in both the total basicity and the distribution of base sites were observed. K-zeolite A exhibited a substantial increase in total basicity (216.4 µmol $CO_2/g_{catalyst}$), together with a significant increase in medium base sites. This behavior can be attributed to the incorporation of K^+ species, which increase the electron density of neighboring oxygen atoms and promote the formation of additional accessible basic sites. In contrast, Ca-zeolite A showed a lower total basicity (72.8 µmol $CO_2/g_{catalyst}$), with dominant high-temperature desorption features, suggesting the presence of fewer but relatively stronger CO_2 adsorption sites associated with interactions between Ca^{2+} ions and framework oxygen atoms.

When compared with the NH_3-TPD results, the modification with K^+ and Ca^{2+} clearly altered the balance and distribution of acid and base sites in the zeolite framework. The presence of stronger and more accessible basic sites is expected to facilitate hydrogen abstraction from ethanol molecules, while the modification of acidic sites may help suppress dehydration side reactions, such as ethylene formation. Therefore, the incorporation of alkali (K^+) and alkaline earth (Ca^{2+}) cations effectively tuned the acid-base properties of zeolite A, resulting in a surface environment more favorable for selective ethanol dehydrogenation.

3.2 Catalytic activity of ethanol dehydrogenation

3.2.1 Reaction study

The effect of temperature on ethanol conversion over zeolite A, K-zeolite A, and Ca-zeolite A in the ethanol dehydrogenation reaction are showed in Figure 8. For all catalysts, ethanol conversion increased with an increase of temperature due to the endothermic characteristic of the dehydrogenation process. The zeolite A possessed the highest ethanol conversion of 68.6% at 400°C. Ca-zeolite A showed slightly

lower ethanol conversion compared to zeolite A, suggesting that calcium modification moderately reduced the catalytic activity. In contrast, K-zeolite A exhibited significantly lower ethanol conversion throughout the temperature range, achieving only about 35.2% at 400°C. This decrease in activity is attributed to the reduced surface acidity and increased basicity of K-zeolite A, as confirmed by NH_3-TPD and CO_2-TPD analyses. The results indicate that the catalytic activity in ethanol dehydrogenation strongly depends on the acid-base characteristics of the zeolite surface, which can be effectively tuned by metal modification. No significant deactivation or change in product selectivity was observed within the experimental time-on-stream under steady-state conditions.

Figure 9 illustrates the product distribution obtained from zeolite A, K-zeolite A, and Ca-zeolite A catalysts in the ethanol dehydrogenation reaction. All catalysts produced ethylene, acetaldehyde (Acetal), and diethyl ether (DEE) with different selectivity depending on reaction temperatures. Although, zeolite A showed the highest ethanol conversion as mentioned above, the selectivity to acetaldehyde was moderate due to the concurrent formation of dehydration products such as ethylene and DEE. Ca-zeolite A also displayed a similar trend as seen for the zeolite A having slightly lower conversion and selectivity, indicating that calcium modification partially altered the acid-base balance on the catalyst surface. In contrast, K-zeolite A demonstrated a distinct catalytic behavior, exhibiting the highest selectivity toward acetaldehyde. Although its overall ethanol conversion was somewhat lower than that of zeolite A, nearly all converted ethanol was selectively transformed into acetaldehyde. This result indicates that potassium incorporation effectively promotes the dehydrogenation pathway, while suppressing the dehydration reaction. The CO_2-TPD analysis supports this finding, revealing enhanced surface basicity after potassium modification. The increased basic sites facilitate α-hydrogen abstraction from ethanol molecules and inhibit acid-catalyzed dehydration reactions. Therefore, the superior performance of K-zeolite A highlights the crucial role of surface basicity in directing ethanol dehydrogenation selectively toward acetaldehyde formation.

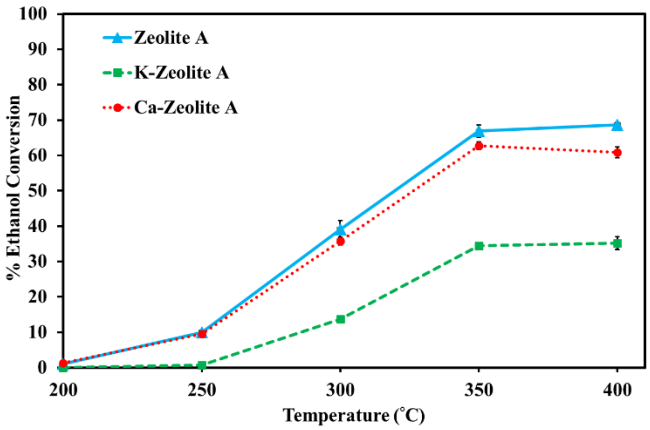

Figure 8. Ethanol conversion (A) over zeolite A, K-zeolite A, and Ca-zeolite A catalysts toward ethanol dehydrogenation. Catalysts: 0.1 g; Pretreated at 200°C for 1 h; Vaporized: 120°C; Feed rate: 0.397 mL·h^{-1}; Reactions temperature: 200°C, 250°C, 300°C, 350°C, and 400°C.

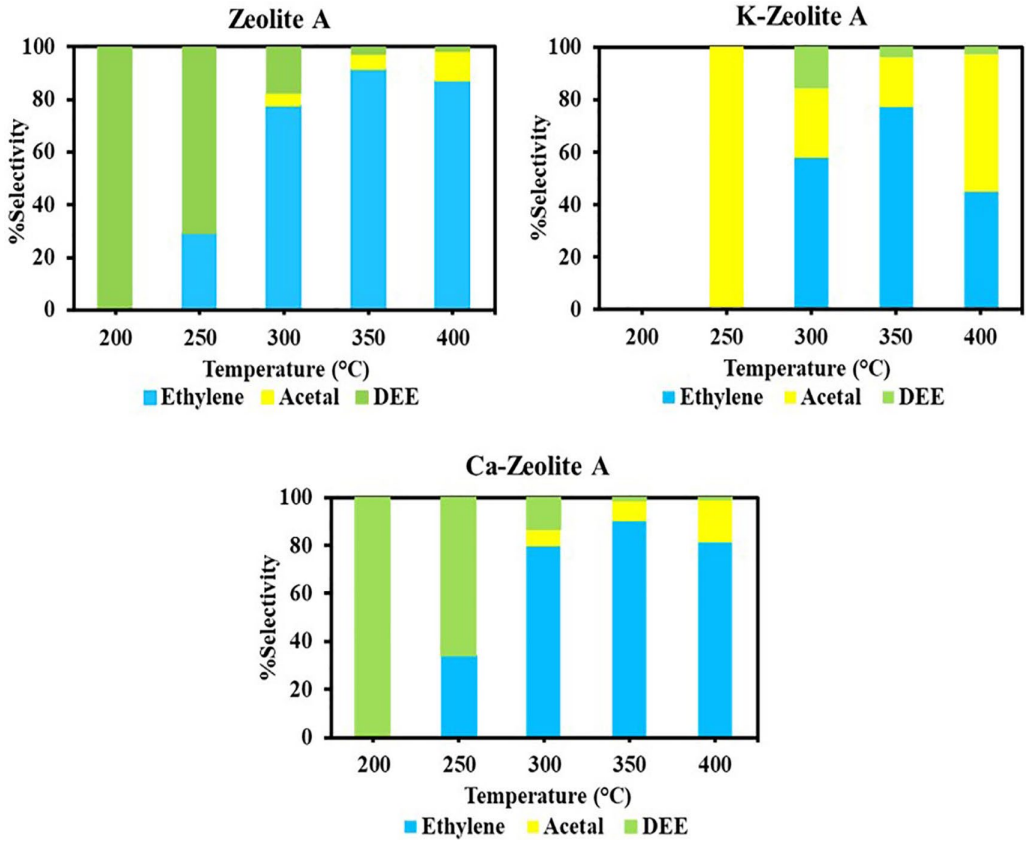

Figure 9. Ethanol conversion and selectivity of acetaldehyde on zeolite A, K-zeolite A, and Ca-zeolite A catalysts toward ethanol dehydrogenation. Catalysts: 0.1 g; Pretreated at 200°C for 1 h; Vaporized: 120°C; Feed rate: 0.397 mL·h^{-1}; Reactions temperature: 200°C, 250°C, 300°C, 350°C, and 400°C.

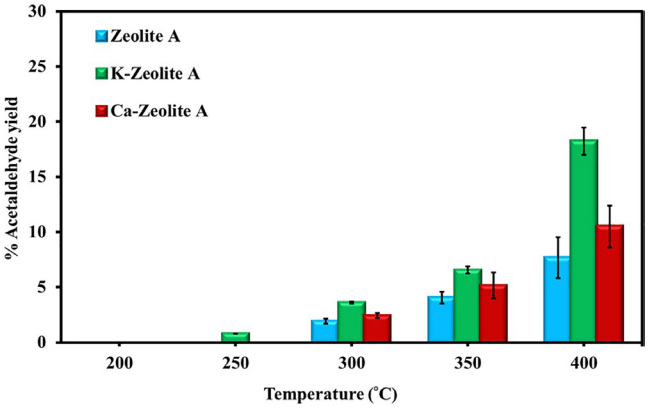

Figure 10. Yield of acetaldehyde over zeolite A, K-zeolite A, and Ca-zeolite A catalysts toward ethanol dehydrogenation. Catalysts: 0.1 g; Pretreated at 200°C for 1 h; Vaporized: 120°C; Feed rate: 0.397 mL·h^{-1}; Reactions temperature: 200°C, 250°C, 300°C, 350°C, and 400°C.

The acetaldehyde yield obtained from ethanol dehydrogenation over zeolite A, K-zeolite A, and Ca-zeolite A catalysts at various reaction temperatures is represented in Figure 10. For all types of catalyst, the acetaldehyde yield increased with temperature, reflecting the endothermic nature of the dehydrogenation reaction. The K-zeolite A exhibited the highest acetaldehyde yield at 400°C, followed by Ca-zeolite A and zeolite A. The higher performance of K-zeolite A can be associated to its moderate surface basicity and well-balanced acid-base properties, which facilitate ethanol activation and dehydrogenation, while suppressing side reactions such as dehydration. In contrast, zeolite A and Ca-zeolite A showed relatively lower yields, likely due to their stronger acidity that favors dehydration pathways. These results demonstrate that potassium modification effectively enhances the selectivity and catalytic performance of zeolite A toward acetaldehyde formation. The catalytic performance of the synthesized K- and Ca-modified zeolite A was compared with other reported noble-metal-free systems to highlight its efficacy. Unlike conventional Al-based zeolites (e.g., H-ZSM-5), which possess strong Brønsted acid sites that predominantly drive ethanol dehydration toward ethylene, our K-modified LTA zeolite shifts the selectivity toward acetaldehyde via a dehydrogenation pathway. Furthermore, compared to bulk Mg-based catalysts such as MgO, which typically require operating temperatures above 400°C to achieve significant conversion [22], our K-zeolite A exhibits competitive activity at lower thermal regimes. This suggests that the hierarchical structure of SCBA-derived zeolite A provides a superior environment for the dispersion of alkali/alkaline-earth cations, leading to more accessible basic sites for the selective abstraction of hydrogen from ethanol.

3.3 Proposed mechanism of ethanol dehydrogenation on K and Ca-modified zeolite A

The proposed pathway for ethanol dehydrogenation over K- and Ca-modified zeolite A is illustrated in Scheme 2. The mechanism involves coordinated bifunctional pathways between the extra-framework cations (Mn^+; K^+ or Ca^{2+}) and the basic framework oxygen atoms.

Initially, the ethanol molecule undergoes adsorption where its oxygen atom coordinates with the cation, acting as a Lewis acid site. Simultaneously, the hydroxyl hydrogen of ethanol interacts with a nearby basic framework oxygen through hydrogen bonding. This synergistic interaction facilitates the deprotonation of the O-H bond, leading to the formation of a surface-bound ethoxide intermediate (CH_3CH_2O*) and a protonated framework oxygen site.

The rate-determining step involves the cleavage of the α-C-H bond (also referred to as α-H abstraction). A neighboring basic framework oxygen abstracts the hydrogen from the α-carbon of the ethoxide species. This step leads to the formation of acetaldehyde, which is weakly adsorbed and readily desorbs from the K^+ or Ca^{2+} sites due to its lower polarity compared to ethanol.

The modification with K^+ and Ca^{2+} is crucial here; these non-redox cations increase the electron density of the framework oxygen atoms, enhancing their basicity and ability to abstract protons. Specifically, the divalent Ca^{2+} provides a stronger electrostatic field that polarizes the ethanol molecule more effectively than monovalent K^+. However, the superior catalytic performance of K^+-modified zeolite A observed in this study (Figure 10) suggests that surface basicity and active site density play a more dominant role. The lower electronegativity of K^+ enhances the electron density of the neighboring framework oxygen to a greater extent than Ca^{2+}, providing stronger basic sites for the rate-determining α-H abstraction. Furthermore, the monovalent nature of K^+ allows for a higher numerical density of cation sites within the LTA framework to balance the framework charge, collectively leading to the observed higher acetaldehyde yield [61-63]. Finally, the surface hydrogen species recombine to release H_2 gas, regenerating the basic active sites for the subsequent catalytic cycle [22,62,64], as illustrated in Scheme 2.

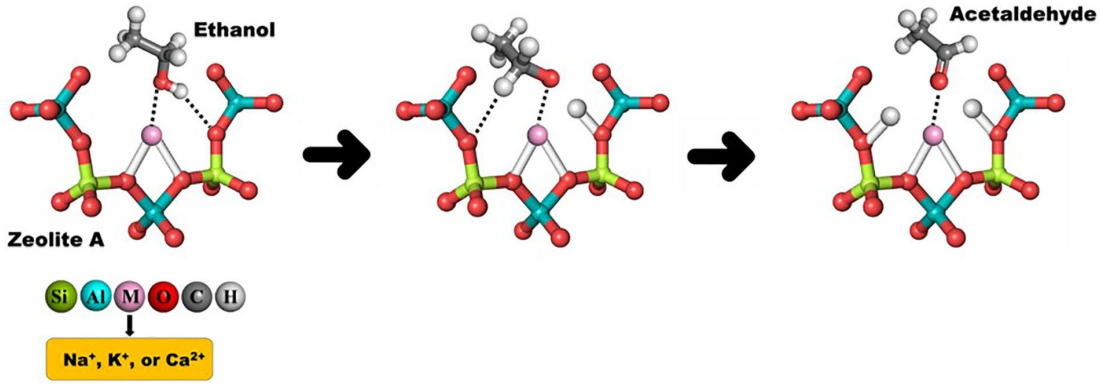

Scheme 2. A conceptual model for the ethanol dehydrogenation over zeolite A, K-zeolite A, and Ca-zeolite A catalysts.

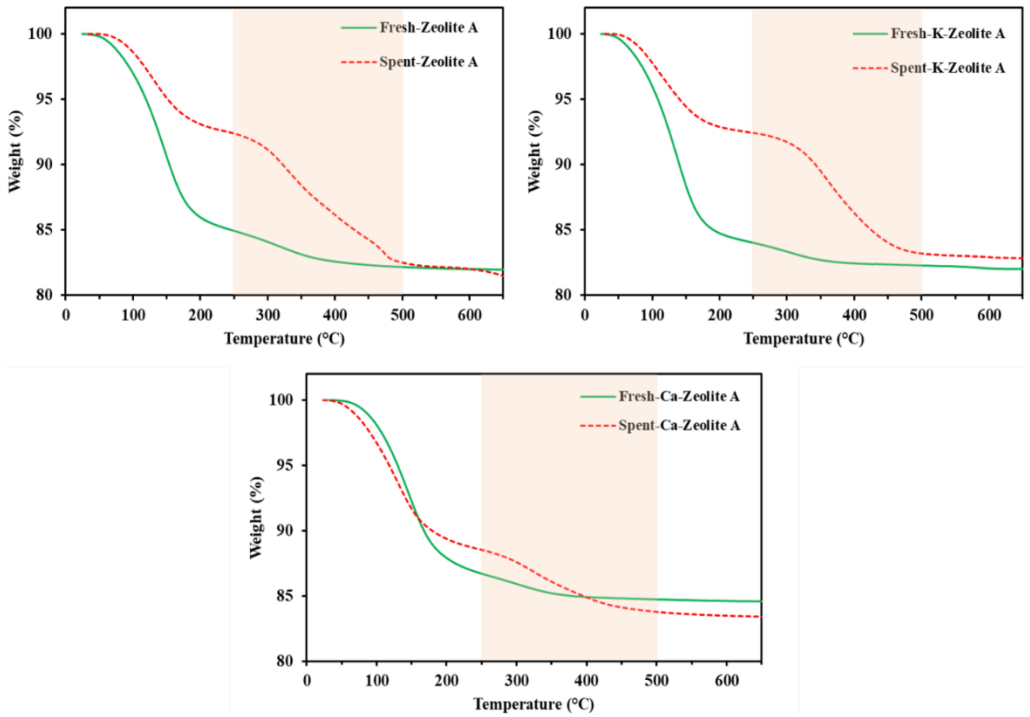

Figure 11. TGA curves of fresh and spent zeolite A, K-zeolite A, and Ca-zeolite A catalysts.

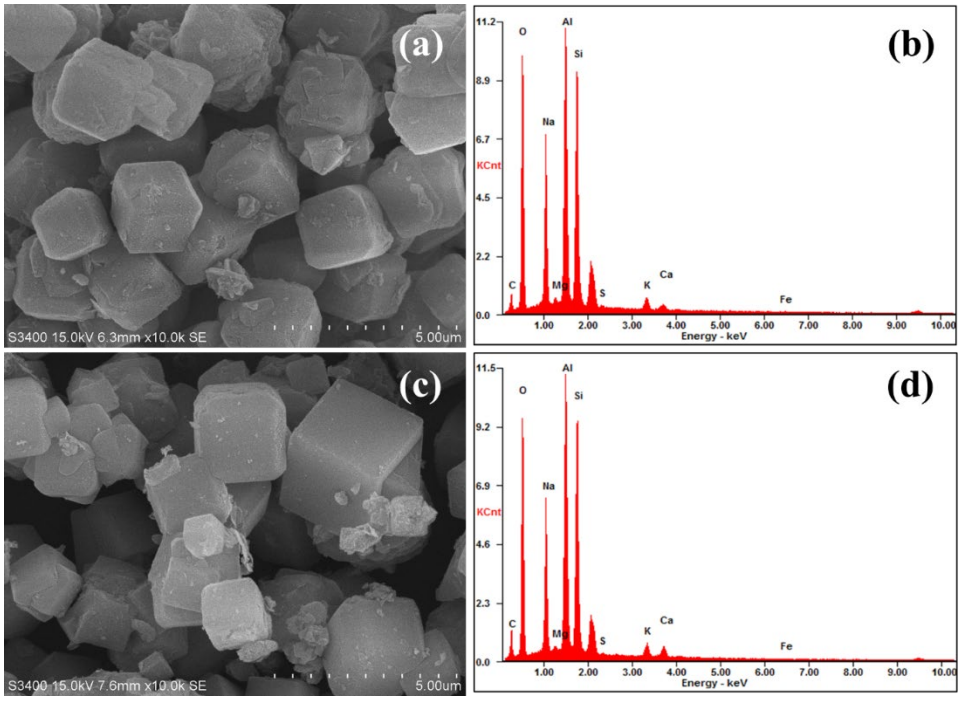

Figure 12. SEM-EDX analysis of 1%K-zeolite A: (a, b) fresh catalyst and (c, d) spent catalyst after reaction.

Table 6. SEM-EDX elemental composition of 1% K-zeolite A before and after ethanol dehydrogenation.

Element	Fresh Catalyst (wt%)	Spent Catalyst (wt%)
%C	6.70	8.28
%Si	23.30	24.19
%Al	21.99	22.98
%O	30.52	27.04
%Na	12.79	11.32
%K	2.07	2.40
%Ca	1.26	2.27

3.4 Post-reaction characterization

Post-reaction characterization was performed to evaluate carbon deposition on the catalysts after the ethanol dehydrogenation reaction. TGA analysis revealed that all fresh catalysts exhibited an initial weight loss below approximately 200°C, which was attributed to the removal of physically adsorbed water. Compared with their corresponding fresh catalysts, the spent catalysts showed additional weight loss in the temperature range of approximately 250°C to 500°C, which is associated with the decomposition of carbonaceous deposits formed during the catalytic reaction.

Among the catalysts studied, the spent K-zeolite A catalyst exhibited the most pronounced additional mass loss within this temperature range, suggesting a relatively higher extent of carbon deposition. In contrast, the difference between the fresh and spent Ca-zeolite A catalysts was less significant, indicating comparatively lower coke formation under the reaction conditions. These results suggest that the acid-base properties of the catalysts may influence the formation of carbonaceous intermediates during ethanol dehydrogenation.

Post-reaction characterization of 1% K-zeolite A was performed using SEM-EDX analysis (Figure 12 and Table 6). The carbon content increased from 6.70 wt% in the fresh catalyst to 8.28 wt% in the spent catalyst, suggesting the formation of carbonaceous deposits during the reaction. This observation is consistent with the TGA results, which showed additional weight loss for the spent catalyst in the temperature range of approximately 250°C to 500°C, attributed to the decomposition of carbonaceous species formed during catalytic operation. Although slight variations in elemental composition were observed after the reaction, these changes are within the typical uncertainty associated with localized EDX measurements. The catalyst composition remained relatively unchanged after catalytic operation.

4. Conclusions

Zeolite A synthesized from sugarcane bagasse ash was successfully modified with K^+ and Ca^{2+} ions to develop catalysts for ethanol dehydrogenation to acetaldehyde. Structural and morphological analyses confirmed that the LTA framework remained intact after cation incorporation, while acidity-basicity measurements revealed significant modifications to the surface properties. Potassium incorporation greatly enhanced the basicity of zeolite A and effectively reduced acidity, creating an optimal surface environment for selective ethanol dehydrogenation. As a result, K-zeolite A exhibited the highest acetaldehyde selectivity (51.8%) and the greatest acetaldehyde yield among the catalysts tested. This study demonstrates that simple cation modification of SCBA-derived zeolite A provides an effective, low-cost, and sustainable alternative to traditional transition-metal-based catalysts used for ethanol dehydrogenation. The ability of non-redox alkali and alkaline-earth cations to tune acid-base characteristics and promote selective acetaldehyde formation opens new avenues for designing environmentally benign catalysts. These findings confirmed the potential of agricultural waste-derived zeolites for green chemical production and contribute valuable insight into catalyst design strategies for ethanol upgrading.

Acknowledgments

The research on “Role of Alkali and Alkaline-Earth doped in zeolite A-derived from Industrial Waste toward Direct Ethanol Dehydrogenation to Acetaldehyde” by Ubon Ratchathani University, Department of Applied Chemistry, has received funding support from the National Science, Research and Innovation Fund (NSRF). The Thailand Graduate Institute of Science and Technology (TGIST) (SCA-CO-2565-17147-TH) is acknowledged for financial support to D. Sukchit. Additional support from Ubon Ratchathani University and the Center of Excellence for Innovation in Chemistry (PERCH-CIC), Ministry of Higher Education, Science, Research and Innovation, is also acknowledged. The National Metal and Materials Technology Center and the National Science and Technology Development Agency (NSTDA) are sincerely appreciated for their contribution. We also thank Mitr Phol Sugar Factory, Amnat Charoen Province, for providing the sugarcane bagasse ash used in this study. This research is supported by Thailand Science and Innovation (TSRI) Fundamental Fund, fiscal year 2026, awarded to S. Boonyuen. This work was supported by the Thailand Science Research and Innovation Fundamental Fund (TU-FF15/2569).

References

[1] Y. Klinthongchai, P. Praserthdam, and B. Jongsomjit, "Synthesis and characteristics of mesoporous carbon catalysts via sulfonation process from surfactant residue and their catalytic properties toward gas-phase ethanol dehydrogenation," *Journal of the Taiwan Institute of Chemical Engineers,* vol. 141, p. 104595, 2022.

[2] J. Ob-eye, P. Praserthdam, and B. Jongsomjit, "Dehydrogenation of ethanol to acetaldehyde over different metals supported on carbon catalysts," *Catalysts*, vol. 9, no. 1, p. 66, 2019.

[3] D. Yu, W. Dai, G. Wu, N. Guan, and L. Li, "Stabilizing copper species using zeolite for ethanol catalytic dehydrogenation to acetaldehyde," *Chinese Journal of Catalysis,* vol. 40, no. 9, pp. 1375–1384, 2019.

[4] M. Okamoto, and Y. Taniguchi, "Wacker-type oxidation in vapor phase using a palladium–copper chloride catalyst in a liquid polymer medium supported on silica gel," *Journal of Catalysis,* vol. 261, no. 2, pp. 195–200, 2009.

[5] A. D. Silva, M. L. Patitucci, H. R. Bizzo, E. D'Elia, and O. A. C. Antunes, "Wacker $PdCl_2$–$CuCl_2$ catalytic oxidation process: Oxidation of limonene," *Catalysis Communications,* vol. 3, no. 9, pp. 435–440, 2002.

[6] R. Jira, "Acetaldehyde from ethylene-a retrospective on the discovery of the wacker process," *Angewandte Chemie International Edition,* vol. 48, no. 48, pp. 9034–9037, 2009.

[7] J.-L. Wang, L.-N. He, C.-X. Miao, and Y.-N. Li, "Ethylene carbonate as a unique solvent for palladium-catalyzed wacker oxidation using oxygen as the sole oxidant," *Green Chemistry,* vol. 11, no. 9, pp. 1317–1320, 2009.

[8] C. H. Christensen, B. Jorgensen, J. Rass-Hansen, K. Egeblad, R. Madsen, S. Kegnaes, S. M. Hansen, M. R. Hansen, H. C. Andersen, and A. Riisager, "Formation of acetic acid by aqueous-phase oxidation of ethanol with air in the presence of a heterogeneous gold catalyst," *Angewandte Chemie International Edition,* vol. 45, no. 28, pp. 4648–4651, 2006.

[9] E. A. Redina, A. A. Greish, I. V. Mishin, G. I. Kapustin, O. P. Tkachenko, O. A. Kirichenko, and L. M. Kustov, "Selective oxidation of ethanol to acetaldehyde over Au–Cu catalysts

prepared by a redox method," *Catalysis Today,* vol. 241, pp. 246–254, 2015.

[10] C. Liu, X. Wang, X. Gao, Y. Wu, X. Wang, F. Song, J. Zhang, Y. Han, and Q. Zhang, "Low-temperature oxidation of ethanol to acetaldehyde over Mo-based catalysts," *RSC Advances,* vol. 15, no. 1, pp. 559-567, 2025.

[11] Y. Gucbilmez, T. Dogu, and S. Balci, "Ethylene and acetaldehyde production by selective oxidation of ethanol using mesoporous V−MCM-41 catalysts," *Industrial & Engineering Chemistry Research,* vol. 45, no. 10, pp. 3496–3502, 2006.

[12] J. Xu, X.-C. Xu, X.-J. Yang, and Y.-F. Han, "Silver/hydroxyapatite foam as a highly selective catalyst for acetaldehyde production via ethanol oxidation," *Catalysis Today,* vol. 276, pp. 19–27, 2016.

[13] P. J. Reeve, and H. J. Fallowfield, "Natural and surfactant modified zeolites: A review of their applications for water remediation with a focus on surfactant desorption and toxicity towards microorganisms," *Journal of Environmental Management,* vol. 205, pp. 253–261, 2018.

[14] D. Sukchit, M. Prajuabsuk, S. Lumlong, C. Inntam, A. Punkvang, S. Wattanarach, P. Thavorniti, B. Jongsomjit, K. Wongyai, D. Gleeson, P. Shanmugam, S. Boonyuen, and P. Pungpo, "Synthesis and characterization of zeolite A from industrial fly ash as a green, cost-effective Cd^{2+} and Pb^{2+} adsorbent for wastewater applications," *ACS Omega,* vol. 10, no. 6, pp. 5981−5992, 2025.

[15] F. Collins, A. Rozhkovskaya, J. G. Outram, and G. J. Millar, "A critical review of waste resources, synthesis, and applications for Zeolite LTA," *Microporous and Mesoporous Materials,* vol. 291, p. 109667, 2020.

[16] V. Verdoliva, M. Saviano, and S. De Luca, "Zeolites as acid/basic solid catalysts: Recent synthetic developments," *Catalysts*, vol. 9, no. 3, p. 248, 2019.

[17] A. Radulović, V. Dondur, R. Dimitrijević, and D. Arandjelović, "Thermal transformation of Na-LTA zeolite into low-carnegieite: The influence of residual sodium and aluminium species," *Thermochimica Acta,* vol. 511, no. 1, pp. 37–42, 2010.

[18] R. Pulikkal Thumbayil, D. B. Christensen, J. Mielby, and S. Kegnæs, "Dehydrogenation of bioethanol using Cu nanoparticles supported on N-doped ordered mesoporous carbon," *ChemCatChem,* vol. 12, no. 22, pp. 5644–5655, 2020.

[19] G. Pampararo, G. Garbarino, A. Comite, G. Busca, and P. Riani, "Acetaldehyde production by ethanol dehydrogenation over Cu-$ZnAl_2O_4$: Effect of catalyst synthetic strategies on performances," *Chemical Engineering Science,* vol. 261, p. 117937, 2022.

[20] G. Li, S. Ma, F. Liu, Z. Wang, and Y. Zhang, "Economic assessment of acetaldehyde production from oxidative dehydrogenation of bioethanol through chemical looping air separation," *Sustainable Energy Technologies and Assessments,* vol. 70, p. 103967, 2024.

[21] G. Pampararo, Z. Hlavenková, A. Styskalik, and D. P. Debecker, "Suppressing on-stream deactivation of $CuSiO_2$ catalysts in the dehydrogenation of bioethanol to acetaldehyde," *Catalysis Science & Technology,* vol. 14, no. 17, pp. 4912–4926, 2024.

[22] H. T. Abdulrazzaq, A. Rahmani Chokanlu, B. G. Frederick, and T. J. Schwartz, "Reaction kinetics analysis of ethanol dehydrogenation catalyzed by MgO–SiO_2," *ACS Catalysis,* vol. 10, no. 11, pp. 6318–6331, 2020.

[23] M. Zhang, Z. Ma, L. Yuan, H. Li, G. Fan, and F. Li, "Defect-mediated MgO-TiO_x hybrid composite anchored single-atom Cu catalysts for enhanced bioethanol upgrading," *Applied Catalysis B: Environment and Energy,* vol. 383, p. 126134, 2026.

[24] E. Spennati, G. Pampararo, G. Garbarino, and P. Riani, "(Ni,Cu) and Cu supported over alumina for ethanol dehydrogenation: effect of preparation, activation, and operando studies," *Applied Catalysis B: Environment and Energy,* pp. 126267, 2025.

[25] G. Giannakakis, A. Trimpalis, J. Shan, Z. Qi, S. Cao, J. Liu, J. Ye, J. Biener, and M. Flytzani-Stephanopoulos, "NiAu single atom alloys for the non-oxidative dehydrogenation of ethanol to acetaldehyde and hydrogen," *Topics in Catalysis,* vol. 61, no. 5–6, pp. 475-486, 2018.

[26] Q. Wang, J. D. Duan, T. Goetjen, J. Hupp, and J. Notestein, "Bimetallic NiCu catalysts supported on a Metal-Organic framework for Non-oxidative ethanol dehydrogenation," *Journal of Catalysis,* vol. 422, pp. 86–98, 2023.

[27] K. Gao, J. Mielby, and S. Kegnæs, "Catalytic dehydrogenation of ethanol over zinc-containing zeolites," *Catalysis Today,* vol. 405-406, pp. 144–151, 2022.

[28] G. Garbarino, P. Riani, M. Villa García, E. Finocchio, V. Sanchez Escribano, and G. Busca, "A study of ethanol dehydrogenation to acetaldehyde over copper/zinc aluminate catalysts," *Catalysis Today,* vol. 354, pp. 167–175, 2020.

[29] C. Wang, G. Garbarino, L. F. Allard, F. Wilson, G. Busca, and M. Flytzani-Stephanopoulos, "Low-temperature dehydrogenation of ethanol on atomically dispersed gold supported on ZnZrOx," *ACS Catalysis,* vol. 6, no. 1, pp. 210–218, 2016.

[30] T. Maihom, M. Probst, and J. Limtrakul, "Density functional theory study of the dehydrogenation of ethanol to acetaldehyde over the Au-exchanged ZSM-5 zeolite: Effect of surface oxygen," *The Journal of Physical Chemistry C,* vol. 118, no. 32, pp. 18564–18572, 2014.

[31] Y. Guan and E. J. M. Hensen, "Ethanol dehydrogenation by gold catalysts: The effect of the gold particle size and the presence of oxygen," *Applied Catalysis A: General,* vol. 361, no. 1, pp. 49–56, 2009.

[32] E. Behravesh, M. M. Melander, J. Wärnå, T. Salmi, K. Honkala, and D. Y. Murzin, "Oxidative dehydrogenation of ethanol on gold: Combination of kinetic experiments and computation approach to unravel the reaction mechanism," *Journal of Catalysis,* vol. 394, pp. 193–205, 2021.

[33] S. Preedavijitkul, C. Autthanit, S. Jadsadajerm, C. Srijaroen, P. Praserthdam, and B. Jongsomjit, "Investigation on deactivation of Cu-Cr catalyst for direct ethanol dehydrogenation to ethyl acetate, acetaldehyde, and hydrogen," *Journal of the Taiwan Institute of Chemical Engineers,* vol. 147, p. 104895, 2023.

[34] Y. Huang, B. Wang, H. Yuan, Y. Sun, D. Yang, X. Cui, and F. Shi, "The catalytic dehydrogenation of ethanol by heterogeneous catalysts," *Catalysis Science & Technology,* vol. 11, no. 5, pp. 1652–1664, 2021.

[35] M. N. Younis, Z. Ren, C. Li, E. Wang, and J. Li, "Alkali and alkaline earth metals (K, Ca, Sr) promoted Cu/SiO_2 catalyst for hydrogenation of methyl acetate to ethanol," *Catalysts*, vol. 13, no. 2, p. 450, 2023.

[36] K. Awodun, Y. He, C. Wu, and S. Masoudi Soltani, "Catalytic pyrolysis of bio-waste in synthesis of value-added products: A systematic review," *Fuel Processing Technology,* vol. 275, p. 108258, 2025.

[37] J. Oliveira, F. Cunha, and L. Ruotolo, "Synthesis of zeolite from sugarcane bagasse fly ash and its application as a low-cost adsorbent to remove heavy metals," *Journal of Cleaner Production,* vol. 229, pp. 956–963, 2019.

[38] N. Chanka, P. Somchuea, M. Chareonpanich, C. Wattanakit, K, Faungnawakij, G. Rupprechter, and A. Seubsai, "High-efficiency hydrogen sulfide removal using copper (II) nitrate-impregnated ZSM-5 derived from sugarcane bagasse ash," *Colloids and Surfaces A: Physicochemical and Engineering Aspects,* vol. 716, p. 136749, 2025.

[39] A. d. J. Torres, M. B. d. Aguiar, W. J. d. Santos, K. Wang, and D. C. S. Garcia, "The influence of sugarcane bagasse ash on the microstructure of autoclaved cementitious material: Comparative study with amorphous and crystalline silica," *Journal of Materials Research and Technology,* vol. 33, pp. 1309–1321, 2024.

[40] Q. Xu, T. Ji, S.-J. Gao, Z. Yang, and N. Wu, "Characteristics and applications of sugar cane bagasse ash waste in cementitious materials," *Materials*, vol. 12, no. 1, p. 39, 2019.

[41] R. Kueasook, R. Kueasook, N. Rattanachueskul, N. Chanlek, D. Dechtrirat, W. Watcharin, P. Amornpitoksuk, and L. Chuenchom, "Green and facile synthesis of hierarchically porous carbon monoliths via surface self-assembly on sugarcane bagasse scaffold: Influence of mesoporosity on efficiency of dye adsorption," *Microporous and Mesoporous Materials,* vol. 296, p. 110005, 2020.

[42] W. Ji, N. Feng, P. Zhao, S. Zhang, S. Zhang, L. Lan, H. Huang, K. Li, Y. Sun, Y. Li, and Y. Ma, "Synthesis of single-phase zeolite a by coal gasification fine slag from ningdong and its application as a high-efficiency adsorbent for Cu^{2+} and Pb^{2+} in simulated waste water," *ChemEngineering*, vol. 4, no. 4, p. 65, 2020.

[43] P. Trongjitraksa, Y. Klinthongchai, P. Praserthdam, and B. Jongsomjit, "Elucidation on supporting effect of WO_3 over MCF-Si and SBA-15 catalysts toward ethanol dehydration," *Journal of the Taiwan Institute of Chemical Engineers,* vol. 152, p. 105168, 2023.

[44] Y. Klinthongchai, S. Prichanont, P. Praserthdam, and B. Jongsomjit, "Synthesis, characteristics and application of mesocellular foam carbon (MCF-C) as catalyst for dehydrogenation of ethanol to acetaldehyde," *Journal of Environmental Chemical Engineering,* vol. 8, no. 3, p. 103752, 2020.

[45] G. Liu, Y. Lin, L. Zhang, M. Zhang, C. Gu, J. Li, T. Zheng, and J. Chai, "Preparation of NaA zeolite molecular sieve based on solid waste fly ash by high-speed dispersion homogenization-assisted alkali fusion-hydrothermal method and its performance of ammonia-nitrogen adsorption," *Journal of Science: Advanced Materials and Devices,* vol. 9, no. 1, p. 100673, 2024.

[46] E. Papa, M. Minelli, M. C. Marchioni, E. Landi, F. Miccio, A. N. Murri, P. Benito, A. Vaccari, and V. Medri, "Metakaolin-based geopolymer – Zeolite NaA composites as CO_2 adsorbents," *Applied Clay Science,* vol. 237, p. 106900, 2023.

[47] P. Seejandee, N. Osakoo, P. Sereerattanakorn, P. Krukkratoke, C. Keawkumay, C. Pansakdanon, J. Wittayakun, N. Chanlek, K. Deekamwong, and S. Prayoonpokarach, "Comparison of potassium catalysts on zeolite sodium A and X in transesterification of palm oil and active species specification," *Heliyon,* vol. 10, no. 16, p. e35975, 2024.

[48] S. Sumari, S. Arni, A. Santoso, L. P. Sholikah, M. R. Asrori, and A. Budianto, "Contribution of Malang quartzite-based silica in K_2O/zeolite Y catalyst for methyl ester synthesis of off grade crude palm oil," *Heliyon,* vol. 10, no. 13, p. e33563, 2024.

[49] J. López, L. Amodio, M. D. M. A. Doncel, J. Cueto, H. Hernando, M. Mazur, J. Cejka, P. Pizarro, and D. Serrano, "Enhanced oil dehalogenation during catalytic pyrolysis of WEEE-derived plastics over Fe- and Ca-modified zeolites," *Journal of Environmental Chemical Engineering,* vol. 12, no. 1, p. 111790, 2023.

[50] M. E. Küçük, I. Makarava, T. Kinnarinen, and A. Häkkinen, "Simultaneous adsorption of Cu(II), Zn(II), Cd(II) and Pb(II) from synthetic wastewater using NaP and LTA zeolites prepared from biomass fly ash," *Heliyon,* vol. 9, no. 10, p. e20253, 2023.

[51] C. G. Fotsop, A. Lieb, and F. Scheffler, "Core-satellite material based metal-doped zeolite LTA for highly efficient iodine sequestration: Adsorption performance and mechanism," *Inorganic Chemistry Communications,* vol. 183, p. 115742, 2026.

[52] Q. Jing, J. Ye, S. Chen, X. Li, L. Guo, W. Zheng, J. Wang, and Y. Gao, "Adsorption performance and mechanism of hierarchical LTA zeolite for Cs^+ in aqueous," *Results in Engineering,* vol. 28, p. 108200, 2025.

[53] L. Alcaraz, B. Sptillo, C. Iglesias, F. A. Lopez, P. Fernandez, C. Belviso, and A. Urbieta, "LTA zeolite particles functionalized with nanomagnetite for effective recovery of dysprosium from liquid solutions," *Microporous and Mesoporous Materials,* vol. 363, p. 112843, 2024.

[54] L. H. de Oliveira, M. V. Pereira, J. G. Meneguin, M. A. S. D. de Barros, J. F. do Nascimento, and P. A. Arroyo, "Influence of regeneration conditions on cyclic CO_2 adsorption on NaA zeolite at high pressures," *Journal of CO_2 Utilization,* vol. 67, p. 102296, 2023.

[55] J. Madhu, A. Santhanam, and D. Velauthapillai, "Synthesis of "Ice Cube" Shaped zeolite a type and Cu^{2+} ion-exchanged zeolites and study of their CO_2 adsorption performance," *ACS Omega,* vol. 9, no. 46, pp. 45926–45942, 2024.

[56] C. G. Fotsop, A. Lieb, and F. Scheffler, "Tailoring the water vapor adsorption properties by thermal performance analysis of post-synthetically ion-exchanged LTA zeolite derived from Cameroonian kaolin," *Journal of Industrial and Engineering Chemistry,* vol. 155, pp. 683–698, 2025.

[57] M. Thommes, K. Kaneko, A. V. Neimark, J. P. Olivier, F. Rodriquez-Reinoso, J. Rouquerol, and K. S. W. Sing, "Physisorption of gases, with special reference to the evaluation of surface area and pore size distribution (IUPAC Technical Report)," *Pure and Applied Chemistry*, vol. 87, no. 9–10, pp. 1051–1069, 2015.

[58] J. Pérez-Ramírez, C. H. Christensen, K. Egeblad, C. H. Christensen, and J. C. Groen, "Hierarchical zeolites: Enhanced utilisation of microporous crystals in catalysis by advances in materials

design," *Chemical Society Reviews,* vol. 37, no. 11, pp. 2530–2542, 2008.

[59] I. M. S. Anekwe, B. Oboirien, and Y. M. Isa, "Effects of transition metal doping on the properties and catalytic performance of ZSM-5 zeolite catalyst on ethanol-to-hydrocarbons conversion," *Fuel Communications,* vol. 18, p. 100101, 2024.

[60] P. Trongjitraksa, M. Yazdanpanah, M. Fereidooni, P. Praserthdam, and B. Jongsomjit, "Effect of ethanol concentration on the catalytic performance of WO_3/MCF-Si and WO_3/SBA-15 catalysts toward ethanol dehydration to ethylene," *South African Journal of Chemical Engineering,* vol. 51, pp. 180–187, 2025.

[61] C. Krutpijit, S. Suelueam, and B. Jongsomjit, "Highly loaded copper on mesoporous silica as catalysts for acetaldehyde production from ethanol: their synthesis, characteristics, and catalytic properties," *Journal of Chemical Technology & Biotechnology,* vol. 100, no. 4, pp. 754–767, 2025.

[62] J. F. DeWilde, C. J. Czopinski, and A. Bhan, "Ethanol dehydration and dehydrogenation on γ-Al_2O_3: Mechanism of acetaldehyde formation," *ACS Catalysis,* vol. 4, no. 12, pp. 4425–4433, 2014.

[63] E. Hemo, R. Virduk, M. Landau, and M. Herskowitz, "Biogasoline and High alcohols production by one step ethanol conversion on densified MgO catalyst with enhanced concentration of surface active sites," *Chemical Engineering Transactions,* vol. 21, pp. 1243–1248, 2010.

[64] X. Huang, S. Wu, Z. Xiao, D. Kong, T. Liang, X. Li, B. Luo, B. Wang, and L. Zhi, "Predicting the optimal chemical composition of functionalized carbon catalysts towards oxidative dehydrogenation of ethanol to acetaldehyde," *Nano Today,* vol. 44, p. 101508, 2022.